# Effects of microstructure of mesoporous $SnO_2$ powders on their $H_2$ sensing properties

Masahiro Hayashi[1], Takeo Hyodo[1], Yasuhiro Shimizu[2] and Makoto Egashira[2]

*[1]Graduate School of Science and Technology, [2]Department of Materials Science and Engineering, Faculty of Engineering, Nagasaki University, 1-14 Bunkyo-machi, Nagasaki 852-8521, Japan*

**Abstract**

Various mesoporous tin dioxide (m-$SnO_2$) powders were prepared from two kinds of combination of a tin source and a surfactant template, and their $H_2$ sensing properties were investigated. The specific surface area and pore volume of the m-$SnO_2$ powder prepared from $Na_2SnO_3 \cdot 3H_2O$ as a tin source and *n*-cetylpyridinium chloride monohydrate ($C_{16}$PyCl; $(C_5H_5NC_{16}H_{33})Cl \cdot H_2O$) as a template under a fixed pH value of 10 (m-$SnO_2$(1)) were larger than those of the m-$SnO_2$ powders prepared from $SnCl_4 \cdot 5H_2O$ as a tin source and aerosol OT (AOT; $C_{20}H_{37}O_7SNa$) as a template under different pH conditions (m-$SnO_2$(2)-*n*; *n* is the value of pH of the precursor solution). However, the specific surface area of m-$SnO_2$(1) decreased drastically by post-grinding, while m-$SnO_2$(2)-*n* powders with small secondary agglomerates showed only a slight decrease in specific surface area during post-grinding. In addition, m-$SnO_2$(2)-*n* sensors exhibited better $H_2$ response and lower resistance than those of m-$SnO_2$(1) sensor, especially at low operating temperatures, probably because of moderately-developed mesopores which promoted easier diffusion of $H_2$ to the most sensitive region of the surface of $SnO_2$ particles.

*Keywords*: tin dioxide; mesopores; particle size; hydrogen; gas sensor

## 1. Introduction

Currently, several metal oxides with developed porous structure are used as a raw material of semiconductor gas sensors, and effective improvement of their gas sensing properties by various techniques, e.g. grain size reduction [1, 2] and gas-diffusion control [3, 4], has thus far been attempted by various researchers. Among them, ordered mesoporous metal oxides have been of great interest from the viewpoints of their controlled mesoporous structure (2~50 nm in diameter), small crystallite size, large specific surface area, etc. However, poor thermal stability of mesoporous structure of $SnO_2$ synthesized previously [5-8] limits their applications to gas sensors, which are usually operated in a temperature range of 200-500ºC. Thus, we have tried and then

succeeded to develop thermally stable mesoporous tin dioxide (m-$SnO_2$) powders by pretreatment with a phosphoric acid (PA) solution before calcination. They showed much larger specific surface areas (>300 $m^2$ $g^{-1}$ even after calcination at 600ºC) than a conventional $SnO_2$ powder [9-11]. However, the gas sensing properties of the m-$SnO_2$ sensors were not as good as those we expected, probably due to their large secondary agglomerates.

In the present study, therefore, various physical characteristics of such secondary agglomerates were controlled by adjusting the preparation conditions. In addition, the responses to 1000 ppm $H_2$ of the thick film sensors fabricated with the m-$SnO_2$ powders were investigated.

## 2. Experimental

### 2.1. *Preparation of m-$SnO_2$ powders*

Two series of m-$SnO_2$ powders were prepared under the conditions summarized in Table 1. m-$SnO_2$(1) powder was prepared from the precipitate obtained by adjusting the pH of the aqueous precursor solution to 10 using an aqueous HCl solution. The precursor solution contained *n*-cetylpyridinium chloride monohydrate ($C_{16}$PyCl; ($C_5H_5NC_{16}H_{33}$)Cl·$H_2O$) as a template, $Na_2SnO_3$·$3H_2O$ as a tin source and trimethylbenzene (mesitylene; MES), where the concentration of $C_{16}$PyCl was 2 wt% and the molar ratios were [$C_{16}$PyCl]/[$Na_2SnO_3$·$3H_2O$] = 2.0 and [MES]/[$Na_2SnO_3$·$3H_2O$] = 2.5. On the other hand, m-$SnO_2$(2)-*n* powders (*n*: the value of pH of the precursor solution) were prepared from the precipitates obtained with the pH adjustment of the aqueous precursor $SnCl_4$·$5H_2O$ solution in a range of 0.6~6.9 using an aqueous $NH_3$ solution, followed by addition of sodium bis(2-ethylhexyl) sulfosuccinate (aerosol-OT, AOT; $C_{20}H_{37}O_7SNa$) as a template, where the concentration of AOT was 1 wt% and the molar ratio was [AOT]/[$SnCl_4$·$5H_2O$] = 2.0. After aging at 20ºC for 3 days in the solutions, these precipitates were treated with a $3.33\times10^{-2}$ M aqueous phosphoric acid (PA) solution for 2 h to improve the thermal stability. The resultant powders were filtered and washed with deionized water. Then they were dried at 80ºC for 12 h and then calcined at 600ºC for 5 h in air. As for m-$SnO_2$(1), the powder without the PA treatment was also prepared in a similar manner to that described above and is denoted as non-PA/m-$SnO_2$(1). In some cases, the calcined powders were post-ground using an agate mortar, to reduce the size of their large agglomerates. To simplify, the samples with and without post-grinding were labeled with '-PG' and '-N', such as m-$SnO_2$-PG and m-$SnO_2$(1)-N, respectively.

Crystal phase, crystallite size and mesoporous structure of m-$SnO_2$ powders were characterized by X-ray diffraction analysis (XRD; Rigaku, RINT2200V, CuKα). The crystallite size was calculated from the (110) diffraction peak using Scherrer's equation. The specific surface area and pore size distribution were measured by BET and BJH methods using a $N_2$ sorption isotherm

(Micromeritics, Tristar3000).

2.2 *Fabrication of m-$SnO_2$ sensors*

The paste of m-$SnO_2$ powder with or without post-grinding was screen-printed on an alumina substrate, on which a pair of interdigitated Pt electrodes had been printed, to fabricate a thick film sensor. Thereafter they were heated at 550ºC for 5 h. The thickness of the films fabricated with non-PA/m-$SnO_2$(1), m-$SnO_2$(1) and m-$SnO_2$(2)-*n* powders was similar (20~30 μm) to each other, irrespective of the post-grinding. The thick film sensors were used to detect 1000 ppm $H_2$ balanced with air in a temperature range of 250~500ºC. The response was defined as $R_a/R_g$, where $R_a$ and $R_g$ were the sensor resistance in air and in 1000 ppm $H_2$, respectively. Morphology of the surfaces of the thick films was observed by a scanning electron microscope (SEM, Hitachi, S-2250N).

## 3. Results and Discussions

3.1. *Characterization of m-$SnO_2$ powders*

Figure 1 shows XRD patterns of representative powders, i.e. non-PA/m-$SnO_2$(1), m-$SnO_2$(1) and m-$SnO_2$(2)-6.9, before and after calcination at 600ºC for 5 h. The calcined powders without post-grinding were subjected to these XRD measurements. Crystallite size values of all powders before and after the calcination, which were calculated by Scherrer's equation, are shown in Table 2. The XRD patterns of all the as-prepared powders, corresponding to the tetragonal crystal structure, were extremely broad, and any significant changes in crystallite size (1.8~2.3 nm) were hard to be observed among these powders. As for non-PA/m-$SnO_2$(1), diffraction peaks ascribed to tetragonal $SnO_2$ appeared clearly and the crystallite size increased obviously after the calcination. On the other hand, as for m-$SnO_2$(1) and m-$SnO_2$(2)-*n* powders, which were treated with a PA solution, very broad characteristics of the diffraction peaks and then the crystallite size were almost unchanged by the calcination. Thus, it is confirmed again that the crystal growth of m-$SnO_2$(1) and m-$SnO_2$(2)-*n* powders were limited by some sort of phosphorus components formed on the $SnO_2$ surface and/or grain boundaries by the PA treatment.

The crystallite size of all powders with post-grinding is also shown in Table 2. After the grinding in an agate mortar, the crystallite size of non-PA/m-$SnO_2$(1) reduced markedly from 20.4 nm to 15.1 nm. On the other hand, those of m-$SnO_2$(1) and m-$SnO_2$(2)-*n* (2.1~2.9 nm) were not affected by the post-grinding.

Figure 2 shows low-angle XRD patterns of non-PA/m-$SnO_2$(1), m-$SnO_2$(1), m-$SnO_2$(2)-0.6 and m-$SnO_2$(2)-6.9 powders before and after calcination. The calcined powders without post-grinding were also subjected to these XRD measurements. A typical peak indicating the formation of

ordered mesoporous structure was confirmed for non-PA/m-$SnO_2$(1), m-$SnO_2$(1) and m-$SnO_2$(2)-0.6 before calcination. The values of d-spacing, namely the intervals of ordered mesopores, calculated from Bragg equation were 4.2 nm, 4.3 nm and 3.7 nm, respectively. On the other hand, such a peak could not be observed for m-$SnO_2$(2)-6.9. Other m-$SnO_2$(2) powders ($n$ = 3.3~5.7) showed similar patterns to that of m-$SnO_2$(2)-6.9. After calcination, ordered mesoporous structure could not be confirmed clearly by the XRD data for all the powders, as shown in Fig. 2(II). Then, the mesoporous structure of the calcined powders was characterized by utilizing the $N_2$ adsorption-desorption properties.

Figure 3 shows $N_2$ adsorption-desorption isotherms and pore size distribution of non-PA/m-$SnO_2$(1)-N, m-$SnO_2$(1)-N and m-$SnO_2$(2)-6.9-N powders. The values of specific surface area of these powders including other m-$SnO_2$(2)-$n$-N powders are listed in Table 3. The adsorption isotherm of non-PA/m-$SnO_2$(1)-N was of type-V, indicating weak interaction between the material and $N_2$ [12]. Then only a small peak was observed around 20 nm in the pore size distribution shown in Fig. 3(b) and the specific surface area was also very small, as summarized in Table 3. On the other hand, the adsorption and desorption isotherms of m-$SnO_2$(1)-N showed little hysteresis, which is classified into type-I [12], and then a large peak at a pore diameter of 1.9 nm was observed in Fig. 3(b). In addition, the specific surface area of m-$SnO_2$(1)-N (365 $m^2$ $g^{-1}$) was much larger than that of non-PA/m-$SnO_2$(1)-N (25 $m^2$ $g^{-1}$). These results confirm again that the PA treatment is very effective in maintaining the well-developed and ordered mesopores and large specific surface area during calcination. As for m-$SnO_2$(2)-6.9-N, a type-IV isotherm was observed with certain hysteresis, which is attributed to a difference between condensation and evaporation processes occurring in pores with narrow necks and wide bodies, i.e. 'ink bottle' pores [12]. Such an isotherm and hysteresis behavior were observed also for other m-$SnO_2$(2)-$n$-N powders. Specific surface areas of m-$SnO_2$(2)-$n$-N powders (115~167 $m^2$ $g^{-1}$) were lower than that of m-$SnO_2$(1)-N (365 $m^2$ $g^{-1}$).

Figure 4 also shows $N_2$ adsorption-desorption isotherms and pore size distribution of non-PA/m-$SnO_2$(1)-PG, m-$SnO_2$(1)-PG and m-$SnO_2$(2)-3.3-PG powders. The values of specific surface area of these powders including other m-$SnO_2$(2)-$n$-PG powders are also listed in Table 3. Comparison of the data shown in Figs. 3, 4 and Table 3 indicates that the post-grinding did not affect so much the $N_2$ adsorption-desorption isotherms, pore size distribution and specific surface area of non-PA/m-$SnO_2$(1). In contrast, the pore volume of m-$SnO_2$(1) and m-$SnO_2$(2)-3.3 was decreased obviously and slightly, respectively, while the pore size of m-$SnO_2$(1) and m-$SnO_2$(2)-3.3 remained almost unchanged. These results may imply that the post-grinding broke only a part of mesopores, but the basic structure of other mesopores was not changed. However, the specific surface area of m-$SnO_2$(1) decreased drastically by the post-grinding, while those of m-$SnO_2$(2)-$n$ decreased slightly.

3.2. *$H_2$ sensing properties of thick film m-$SnO_2$ sensors*

Figure 5 shows response transients of several sensors fabricated with the calcined powders and the post-ground powders. The operating temperature of all the sensors was kept constant at 350ºC. Resistance in air of both m-$SnO_2$(1)-N and m-$SnO_2$(1)-PG sensors ($\log(R_a/\Omega)$ = 6.8~7.4) was much larger than that of non-PA/m-$SnO_2$(1)-PG sensor ($\log(R_a/\Omega)$ = 5.0), probably because of the much small crystallite size and therefore grain size of m-$SnO_2$(1)-N and m-$SnO_2$(1)-PG powders and the existence of some phosphorus components (e.g., $SnP_2O_7$) at the boundaries among the grains. In addition, the values of resistance in air of m-$SnO_2$(2)-6.9-N and m-$SnO_2$(2)-6.9-PG sensor ($\log(R_a/\Omega)$ = 4.5~4.7) were slightly lower than that of non-PA/m-$SnO_2$(1)-PG sensor. This may be due to the difference of a tin source ($Na_2SnO_3 \cdot 3H_2O$ and $SnCl_4 \cdot 5H_2O$) and then the kind of impurities involved in sensors. However, $H_2$ responses of m-$SnO_2$(2)-6.9-N and m-$SnO_2$(2)-6.9-PG sensors ($R_a/R_g$ = 39 and 43, respectively), with lower sensor resistance, were relatively higher than those of non-PA/m-$SnO_2$(1)-PG, m-$SnO_2$(1)-N and m-$SnO_2$(1)-PG sensors ($R_a/R_g$ = 16, 20 and 27, respectively). On the other hand, the post-grinding seems to result in a decrease in sensor resistance both for m-$SnO_2$(1) and m-$SnO_2$(2)-6.9 sensors, especially for m-$SnO_2$(1), while it was ineffective to improve their $H_2$ responses. Thus, it was confirmed that the crystallite size, pore volume and specific surface area of the sensor materials affect the gas sensing properties as well as the sensor resistance in air.

Table 4 shows 90% response and recovery times of the response transients of several sensors fabricated with the calcined powders and the post-ground powders. The operating temperature of all the sensors was again kept at 350ºC. In the case of m-$SnO_2$(2)-*n* sensors, the values of 90% response time were in the range of 28~35 s, irrespective of the post-grinding. However, non-PA/m-$SnO_2$(1)-PG, m-$SnO_2$(1)-N and m-$SnO_2$(1)-PG sensors tended to show a longer response time (84 s, 39 s and 52 s, respectively). In the cases of m-$SnO_2$(1)-N and m-$SnO_2$(1)-PG sensors, longer response times can be ascribed to the smaller pore size and then the larger specific surface area, both of which lead to difficult $H_2$ diffusion inside the mesopores in comparison with that for m-$SnO_2$(2)-*n* sensors. As stated previously, non-PA/m-$SnO_2$(1)-PG showed a very small specific surface area (31 $m^2\ g^{-1}$) and then a less amount of small pores; thus, the response time of the sensor was expected to be short due to rather fast gas diffusion inside the pores and a small number of active sites for $H_2$ detection. But, the results summarized in Table 4 are not coincident with this expectation, although the film thickness of all the sensors is similar to each other (20~30 μm). The reason for this phenomenon is not clear and is the subject in our future research work.

In contrast, 90% recovery times were very long in comparison with 90% response times and varied widely even for the family of m-$SnO_2$(2)-*n* sensors. Especially, non-PA/m-$SnO_2$(1)-PG showed the longest recovery time among the sensors tested. Chemisorbed water, which was produced by the combustion of $H_2$, may have inhibited the formation of oxygen adsorbates to a level of that established under the original air environment, and then led to the longer recovery time than

the response time.

Figure 6 shows the operating temperature dependence of response to 1000 ppm $H_2$ and resistance in air of several sensors fabricated with the calcined powders and the post-ground powders. It is again confirmed that the post-grinding was not effective for improving the $H_2$ gas response properties so much, as shown in Fig. 6. The $H_2$ response of non-PA/m-$SnO_2$(1)-PG sensor (maximum response: $R_a/R_g$ = 16) was extremely lower than those of m-$SnO_2$(1)-N, m-$SnO_2$(1)-PG, m-$SnO_2$(2)-*n*-N and m-$SnO_2$(2)-*n*-PG sensors, probably due to its small specific surface area (31 $m^2$ $g^{-1}$). On the other hand, the values of $H_2$ response of m-$SnO_2$(2)-*n*-PG sensors (maximum response: $R_a/R_g$ = 33~43) were larger than that of m-$SnO_2$(1)-PG sensor (maximum response: $R_a/R_g$ = 27~30), especially at lower operating temperature (350ºC), while the resistance in air of m-$SnO_2$(2)-*n*-PG sensors was relatively lower than that of m-$SnO_2$(1)-PG sensor at all operating temperatures, indicating more active reaction of $H_2$ with chemisorbed oxygen at the surface of m-$SnO_2$(2)-*n*-PG sensor.

Figure 7 shows SEM photographs of the surfaces of m-$SnO_2$(1) and m-$SnO_2$(2)-6.9 sensors fabricated with the calcined powders and the post-ground powders. The surface morphology of other m-$SnO_2$(2)-*n*-N and m-$SnO_2$(2)-*n*-PG sensors is almost similar to those of m-$SnO_2$(2)-6.9-N and m-$SnO_2$(2)-6.9-PG sensors, respectively. Secondary agglomerates of m-$SnO_2$(2)-6.9-PG sensor were extremely smaller than those of m-$SnO_2$(1)-N sensor. As mentioned previously in Fig. 5, the post-grinding of the powders resulted in a decrease in sensor resistance in air. This phenomenon may be explained by the increased number of electrical contact points due to the decreased secondary particles, namely an increase in contact area, and this effect is considered to be superior to the resistance increase which may arise from an increase in the number of Schottky barriers at the interface among the particles. In addition, the resistance reduction of m-$SnO_2$(1) sensor induced by the post-grinding was larger than that of all m-$SnO_2$(2)-*n* sensors (Figs. 5 and 6). This result is also confirmed by the fact that the change in the size of secondary agglomerates observed for m-$SnO_2$(1) was larger than that observed for m-$SnO_2$(2)-*n*, as shown in Fig. 7.

Figure 8 shows the variations of resistance in air at 250ºC and the maximum $H_2$ response of non-PA/m-$SnO_2$(1), m-$SnO_2$(1) and m-$SnO_2$(2)-*n* sensors with their specific surface area. The resistance in air tended to increase with increasing the specific surface area, except for non-PA/m-$SnO_2$(1)-N having the smallest surface area. The much higher resistance of m-$SnO_2$(1)-N and m-$SnO_2$(1)-PG sensors is attributed to their large specific surface area and then a large amount of chemisorbed oxygen in the air environment. On the other hand, the maximum $H_2$ response was obtained with the sensors having a surface area in the range between 122 and 132 $m^2$ $g^{-1}$, irrespective of the post-grinding, and was not obtained with the sensors having a larger specific surface area, i.e. m-$SnO_2$(1)-N and m-$SnO_2$(1)-PG sensors. This tendency may imply that moderately developed mesoporous structure will lead to easier diffusion of $H_2$ to the most sensitive region of the surface of $SnO_2$ particles. In addition, less agglomeration tendency of m-$SnO_2$(2)-*n*

may also be effective for achieving the high $H_2$ gas sensing properties.

Investigation about the effects of phosphorus components, which are extremely important to stabilize the well-developed mesoporous structure of m-$SnO_2$ at elevated temperature, on the gas sensing properties, gas sensitivity and selectivity to various gases such as hydrocarbons and $NO_2$, and long-term stability is of course future subjects. In addition, development of high-functional m-$SnO_2$ materials (e.g., thin mesoporous films oriented to a substrate and uniform nano-particles) are also very important to improve gas sensing properties of m-$SnO_2$ sensors.

## 4. Conclusion

Two series of m-$SnO_2$ powders were prepared (m-$SnO_2$(1) from $Na_2SnO_3 \cdot 3H_2O$ and $C_{16}PyCl$ and m-$SnO_2$(2)-*n* from $SnCl_4 \cdot 5H_2O$ and AOT), and their $H_2$ sensing properties were investigated. PA treatment led to large surface area, large pore volume, well-developed mesoporous structure and small crystallite size, and increased the sensor response to 1000 ppm $H_2$. Post-grinding was not effective in increasing the sensor response. On the other hand, the specific surface area and pore volume of m-$SnO_2$(2)-*n* were smaller than that of m-$SnO_2$(1), while m-$SnO_2$(2)-*n* sensors showed larger response to 1000 ppm $H_2$ than m-$SnO_2$(1) sensor especially at lower operating temperatures. Among all the samples tested, the maximum $H_2$ response was obtained with the sensors having a surface area in the range between 122 and 132 $m^2\ g^{-1}$, irrespective of the post-grinding, probably because the moderately developed mesoporous structure provided easier diffusion of $H_2$ to the most sensitive region of the surface of $SnO_2$ particles.

References


[1] C. Xu, J. Takaki, N. Miura, N. Yamazoe, Relationship between gas sensitivity and maicrostructure of porous $SnO_2$, Denki Kagaku (presently Electrochemistry) 58 (1990) 1143-1148.

[2] C. Xu, J. Takaki, N. Miura, N. Yamazoe, Grain size effects on gas sensitivity of porous $SnO_2$-besed elements, Sens. Actuators B 3 (1991) 147-155.

[3] Y. Shimizu, Y. Nakamura, M. Egashira, Effects of diffusivity of hydrogen and oxygen through pores of thick film $SnO_2$-based sensors on their sensing properties, Sens. Actuators B 13/14 (1993) 128-131.

[4] Y. Shimizu, T. Maekawa, Y. Nakamura, M. Egashira, Effects of gas diffusivity and reactivity on sensing properties of thick film $SnO_2$-based sensors, Sens. Actuators B 46 (1998) 163-168.

[5] N. Uragappan, C.N.R. Rao, Mesoporous phases based on $SnO_2$ and $TiO_2$, Chem. Commun. 14 (1996) 1685-1686.

[6] K.G. Servin, T.M. Abdel-Fattah, T.J. Pinnavaia, Supramolucular assembly of mesostructured tin

oxide, Chem. Commun. 14 (1998) 1471-1472.

[7] F. Chen, M. Liu, Preparation of mesoporous tin oxide for electrochemical application, Chem. Commun. 18 (1999) 1829-1830.

[8] P. Yang, D. Zhao, D.I. Margolese, B.F. Chmelka, G.D. Stucky, Generalized syntheses of large pore mesoporous metal oxide with semicrystalline frameworks, Nature 396 (1998) 152-155.

[9] T. Hyodo, N. Nishida, Y. Shimizu, M. Egashira, Preparation of thermally stable mesoporous tin dioxide powders with high specific surface area by utilizing self-assembly of surfactants, J. Ceram. Soc. Japan 109 (2001) 481-483.

[10] T. Hyodo, N. Nishida, Y. Shimizu, M. Egashira, Preparation and gas-sensing properties of thermally stable mesoporous $SnO_2$, Sens. Actuators B, 83 (2001) 209-215.

[11] T. Hyodo, S. Abe, Y. Shimizu, M. Egashira, Gas-sensing properties of ordered mesoporous $SnO_2$ and effects of coatings thereof, Sens. Actuators B 93 (2003) 590-600.

[12] K.S.W. Sing, D.H. Everett, R.A.W. Haul, L. Mosenu, R.A. Pierotti, J. Rouquerol, T. Siemieniewska, Reporting Physisorption data for gas/solid systems with special reference to the determination of surface area and porosity, Pure Appl. Chem. 57 (1985) 603-619.

**Biographies**

**Masahiro Hayashi** received his B. Eng. Degree and M. Eng. Degree in materials science and engineering from Nagasaki Uniersity in 2007 and 2009, respectively.

**Takeo Hyodo** received his B. Eng. Degree in applied chemistry and M. Eng. Degree in materials science and technology in 1992 and 1994, respectively, and Dr. Eng. Degree in 1997 from Kyushu University. He has been an Assistant Professor at Nagasaki University since 2007. His research interests are the developments of electrochemical devices such as chemical sensors and lithium batteries, and mesoporous and macroporous materials.

**Yasuhiro Shimizu** received his B. Eng. Degree in applied chemistry in 1980 and Dr. Eng. Degree in 1987 from Kyushu University. He has been a Professor at Nagasaki University since 2005. His current research concentrates on development of odor sensors and design of intelligent sensors by controlling gas diffusivity and reactivity.

**Makoto Egashira** received his B. Eng. Degree and M. Eng. Degree in applied chemistry in 1966 and 1968, respectively, and Dr. Eng. Degree in 1974 from Kyushu University. He has been a Professor at Nagasaki University since 1985. His current interests include the development of new chemical sensors, surface modification of ceramics, preparation of hollow ceramic microspheres and porous films and application of microwave-induced plasma.

**Figure captions**

Fig. 1 XRD patterns of non-PA/m-$SnO_2$(1), m-$SnO_2$(1) and m-$SnO_2$(2)-6.9 powders (I) before and (II) after calcination at 600ºC for 5 h.

Fig. 2 Low-angle XRD patterns of non-PA/m-$SnO_2$(1), m-$SnO_2$(1), m-$SnO_2$(2)-0.6 and m-$SnO_2$(2)-6.9 powders (I) before and (II) after calcination at 600ºC for 5 h. The values given at individual peaks are the d-spacings.

Fig. 3 (a) $N_2$ adsorption-desorption isotherms and (b) pore size distribution of non-PA/m-$SnO_2$(1)-N, m-$SnO_2$(1)-N and m-$SnO_2$(2)-6.9-N powders after calcination at 600ºC for 5 h.

Fig. 4 (a) $N_2$ adsorption-desorption isotherms and (b) pore size distribution of non-PA/m-$SnO_2$(1)-PG, m-$SnO_2$(1)-PG and m-$SnO_2$(2)-6.9-PG powders after calcination at 600ºC for 5 h.

Fig. 5 Response transients of several sensors fabricated with calcined powders and post-ground powders (operating temperature: 350ºC).

Fig. 6 Operating temperature dependences of response to 1000 ppm $H_2$ ($R_a/R_g$) and resistance in air ($\log(R_a/\Omega)$) of several sensors fabricated with (a) calcined powders and (b) post-ground powders.

Fig. 7 SEM photographs of the surfaces of m-$SnO_2$(1) and m-$SnO_2$(2)-6.9 sensors fabricated with (a) calcined powders and (b) post-ground powders.

Fig. 8 Variations of resistance in air at 250ºC and maximum response to 1000 ppm $H_2$ of non-PA/m-$SnO_2$(1), m-$SnO_2$(1) and m-$SnO_2$(2)-*n* sensors (●) with and (○) without post-grinding as a function of specific surface area (SSA).

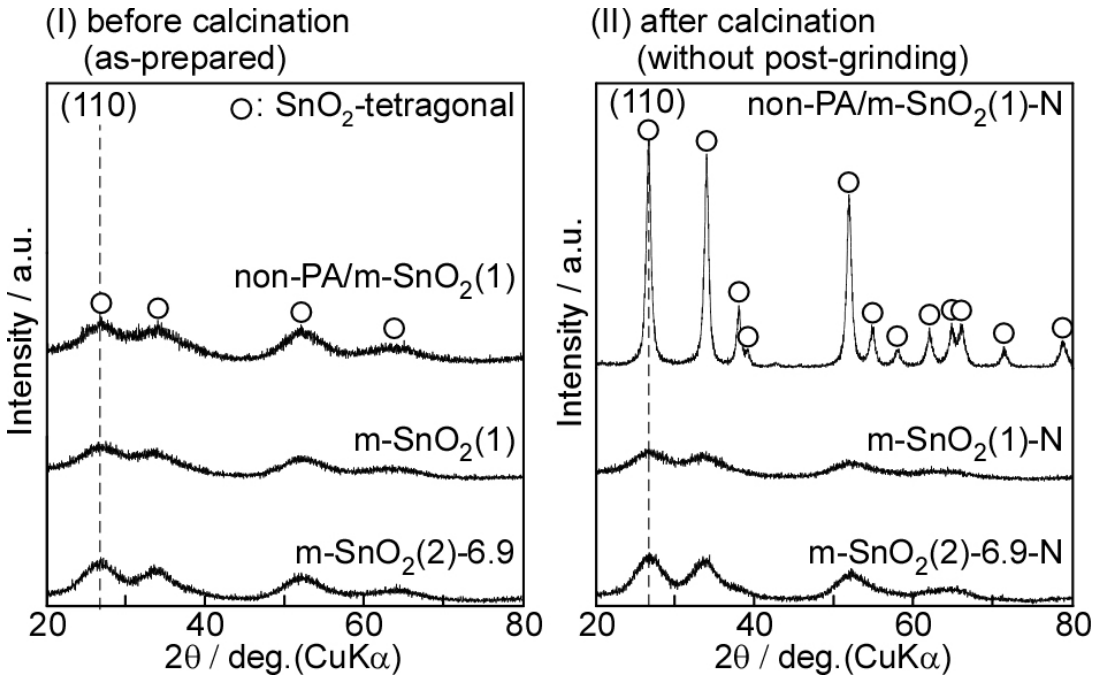


Fig. 1 Hayashi et al.

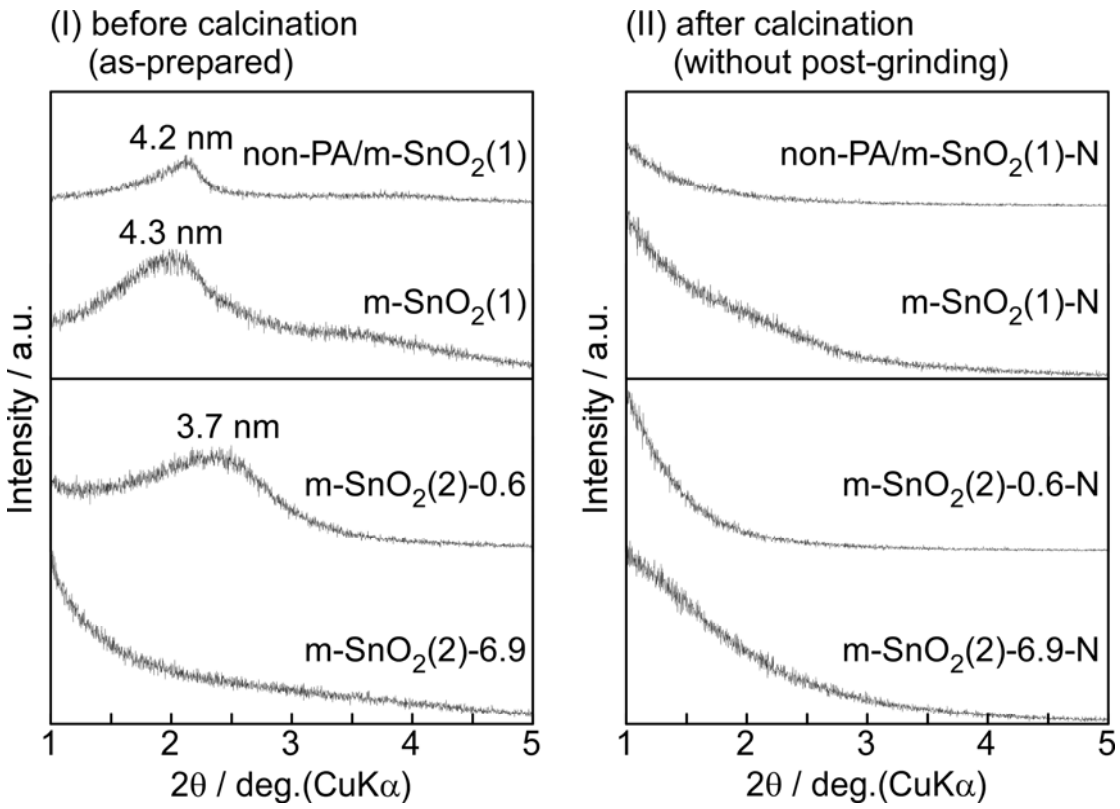


Fig. 2 Hayashi et al.

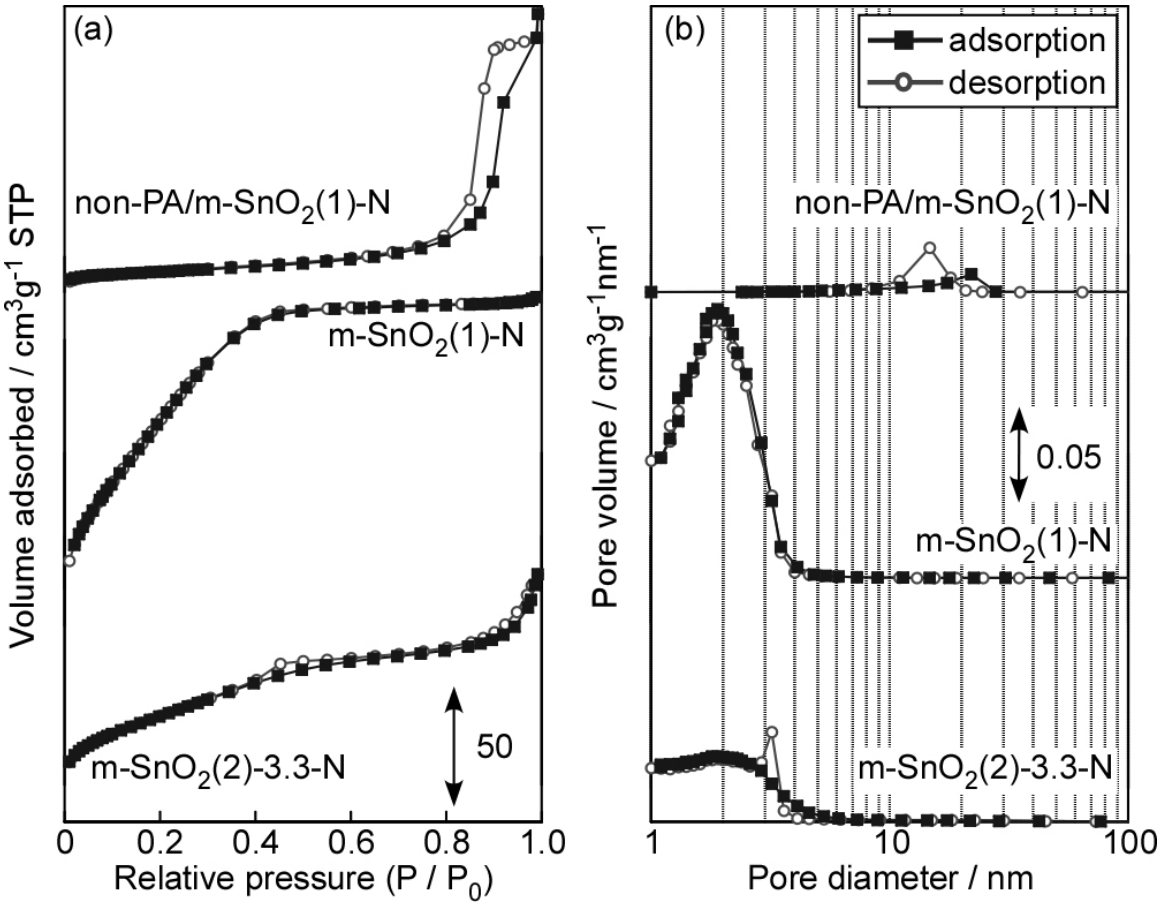


Fig. 3 Hayashi et al.

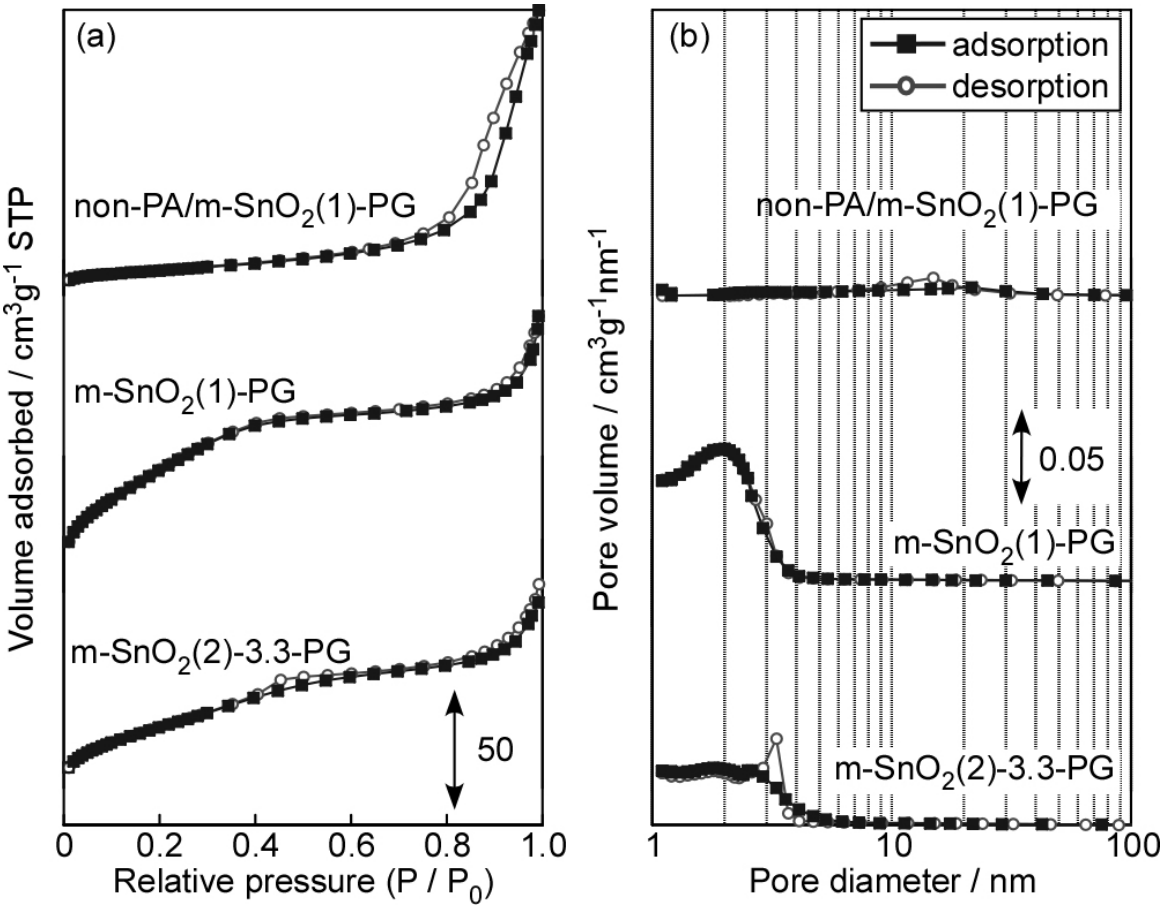


Fig. 4 Hayashi et al.

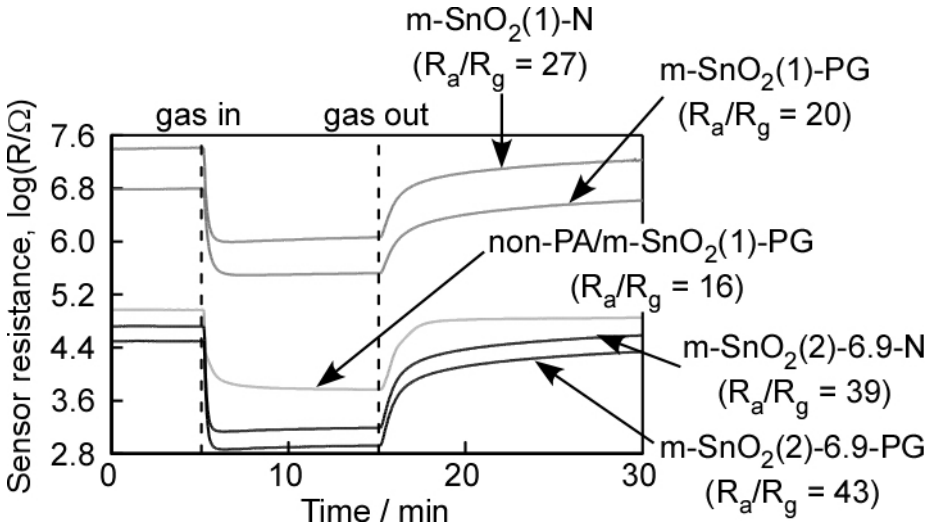


Fig. 5 Hayashi et al.

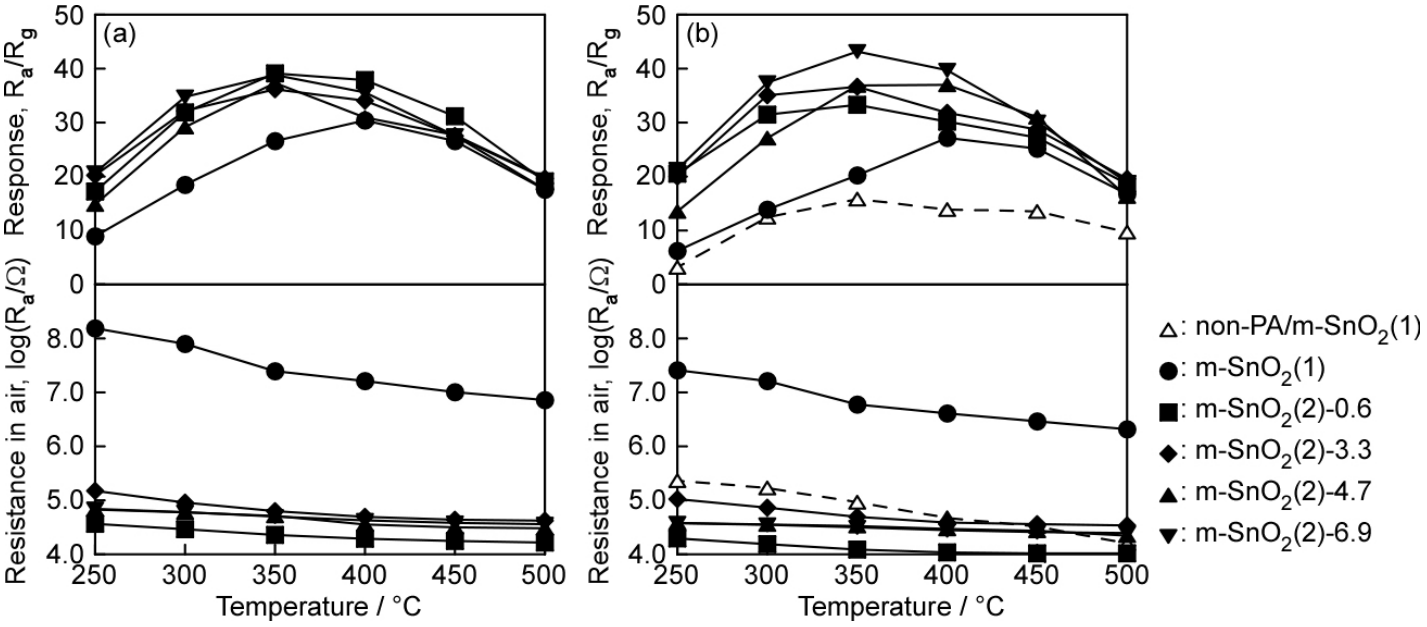


Fig. 6 Hayashi et al.

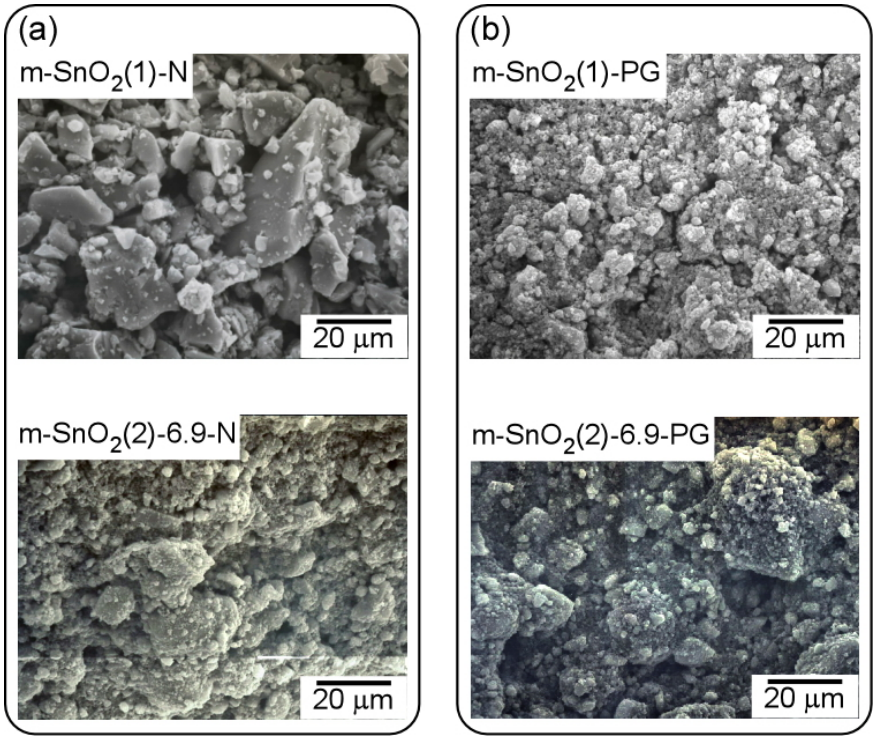


Fig. 7 Hayashi et al.

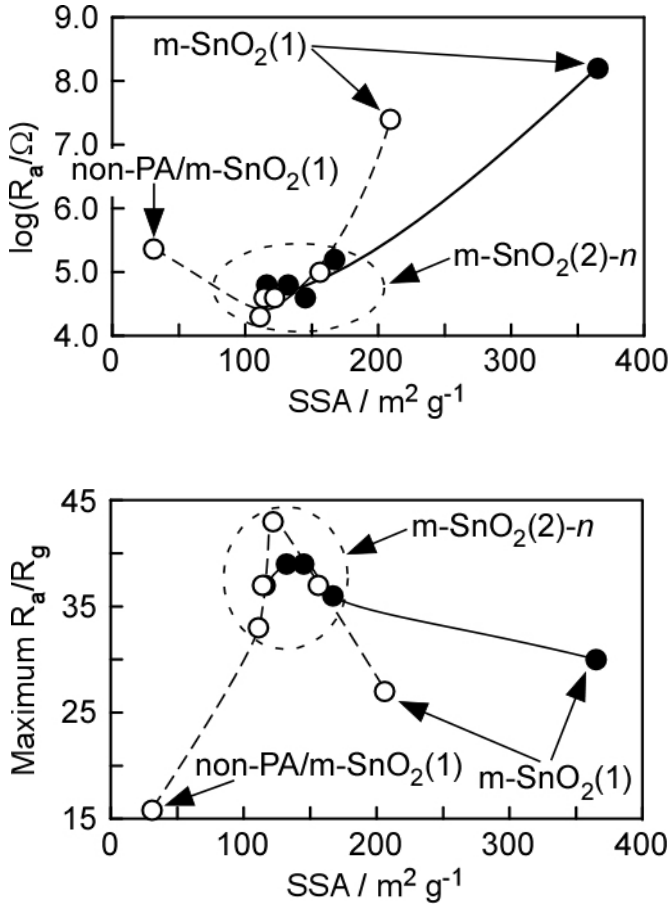


Fig. 8 Hayashi et al.

Table 1 Preparation conditions of non-PA/m-$SnO_2$(1), m-$SnO_2$(1) and m-$SnO_2$(2)-*n* powders.

| Sample | Template (T) and Sn source (S) used | pH | pH-control solution |
|---|---|---|---|
| non-PA/m-$SnO_2$(1) | T: $C_{16}PyCl$ S: $Na_2SnO_3 \cdot 3H_2O$ | 10 | HCl aq. |
| m-$SnO_2$(1) | | | |
| m-$SnO_2$(2)-0.6 | T: AOT S: $SnCl_4 \cdot 5H_2O$ | 0.6 | — |
| m-$SnO_2$(2)-3.3 | | 3.3 | $NH_3$ aq. |
| m-$SnO_2$(2)-4.0 | | 4.0 | |
| m-$SnO_2$(2)-4.7 | | 4.7 | |
| m-$SnO_2$(2)-5.7 | | 5.7 | |
| m-$SnO_2$(2)-6.9 | | 6.9 | |

Table 2 Crystallite size of non-PA/m-$SnO_2$(1), m-$SnO_2$(1) and m-$SnO_2$(2)-*n* powders before and after calcination at 600ºC for 5 h and subsequent post-grinding.

| Sample | Crystallite size / nm | | |
|---|---|---|---|
| | before calcination | after calcination | |
| | | without post-grinding | with post-grinding |
| non-PA/m-$SnO_2$(1) | 2.1 | 20.4 | 15.1 |
| m-$SnO_2$(1) | 1.8 | 1.8 | 2.1 |
| m-$SnO_2$(2)-0.6 | 1.9 | 2.5 | 2.8 |
| m-$SnO_2$(2)-3.3 | 2.3 | 2.8 | 2.9 |
| m-$SnO_2$(2)-4.0 | 2.2 | 2.4 | 2.6 |
| m-$SnO_2$(2)-4.7 | 2.1 | 2.3 | 2.5 |
| m-$SnO_2$(2)-5.7 | 2.2 | 2.4 | 2.5 |
| m-$SnO_2$(2)-6.9 | 2.1 | 2.4 | 2.5 |

Table 3 Specific surface area of non-PA/m-$SnO_2$(1), m-$SnO_2$(1) and m-$SnO_2$(2)-*n* powders after calcination at 600°C for 5 h with and without the post-grinding treatment.

| Sample | Specific surface area / $m^2$ $g^{-1}$ | |
|---|---|---|
| | without post-grinding | with post-grinding |
| non-PA/m-$SnO_2$(1) | 25 | 31 |
| m-$SnO_2$(1) | 365 | 209 |
| m-$SnO_2$(2)-0.6 | 145 | 111 |
| m-$SnO_2$(2)-3.3 | 167 | 156 |
| m-$SnO_2$(2)-4.0 | 130 | 109 |
| m-$SnO_2$(2)-4.7 | 116 | 114 |
| m-$SnO_2$(2)-5.7 | 115 | 118 |
| m-$SnO_2$(2)-6.9 | 132 | 122 |

Table 4 90% response and recovery times of several sensors fabricated with calcined powders and post-ground powders (operating temperature: 350ºC).

| Sample | 90% response time / s | | 90% recovery time / s | |
|---|---|---|---|---|
| | without post-grinding | with post-grinding | without post-grinding | with post-grinding |
| non-PA/m-$SnO_2$(1) | — | 84 | — | > 900 |
| m-$SnO_2$(1) | 39 | 52 | 780 | > 900 |
| m-$SnO_2$(2)-0.6 | 28 | 29 | 470 | 548 |
| m-$SnO_2$(2)-3.3 | 30 | 32 | 697 | 639 |
| m-$SnO_2$(2)-4.7 | 35 | 34 | > 900 | 887 |
| m-$SnO_2$(2)-6.9 | 34 | 34 | 797 | 885 |